Journal of Zhejiang University-SCIENCE B in press
www.jzus.zju.edu.cn; www.springer.com/journal/11585
E-mail: jzus_b@zju.edu.cn

Research Article

https://doi.org/10.1631/jzus.B2600356

Decellularized hard palatal mucosa as a bioactive scaffold for bone regeneration

Jin HE*, Lingfei REN*, Mengdie FU, Qifeng JIANG, Xueting WANG, Zhiwei JIANG✉, Guoli YANG✉

Stomatology Hospital, School of Stomatology, Zhejiang University School of Medicine, Zhejiang Provincial Clinical Research Center for Oral Diseases, Zhejiang Key Laboratory of Oral Biomedical, Engineering Research Center of Oral Biomaterials and Devices of Zhejiang Province, Hangzhou 310000, China

Abstract: Autogenous bone grafting remains the gold standard for bone regeneration, however, its clinical application is limited by restricted availability, donor site morbidity and postoperative complications. Decellularized extracellular matrix (ECM)-based biomaterials have emerged as promising alternatives because of their low immunogenicity and preserved biological properties. In this study, a standardized, time-efficient and reproducible decellularization protocol was derived to prepare a decellularized hard palatal mucosa scaffold (DPM), which was then evaluated for its potential in bone regeneration. Histological staining, DNA quantification, scanning electron microscopy, immunofluorescence, and mass spectrometry demonstrated that DPM effectively removed most cellular components while largely preserving the native ECM architecture and major matrix-associated proteins. In vitro experiments further indicated that DPM supported recellularization, proliferation and osteogenesis-related gene expression. In a rat calvarial defect model, DPM promoted new bone formation. Collectively, these findings suggest that DPM may serve as a promising natural scaffold for bone defect repair, with potential applications in regenerative medicine and tissue engineering.

Key words: Decellularized hard palatal mucosa; Extracellular matrix; Scaffold; Bone regeneration

Unedited

1 Introduction

Owing to its osteogenic, osteoinductive and osteoconductive properties, autogenous bone grafting remains the benchmark for bone defect repair (Huan et al., 2025; Lichte, Pape, Pufe, Kobbe, & Fischer, 2011). Its clinical application, however, is limited by restricted tissue availability, donor site morbidity, and the risk of complications associated with graft harvesting (Szpalski, Barr, Wetterau, Saadeh, & Warren, 2010). Although various synthetic and exogenous scaffolds have shown promising outcomes, they cannot fully reproduce complex biochemical cues, cell–extracellular matrix (ECM) interactions, and the three-dimensional (3D) architecture of native tissues (Bae, Bhang, Kim, & Park, 2012; Jung, Bhuiyan, & Ogle, 2016). ECM-derived biomaterials from human or animal tissues have attracted increasing attention as scaffolds for tissue regeneration (Lau et al., 2019). Decellularization is a technique that removes cellular components and reduces potentially immunogenic materials while preserving the structural and bioactive properties of the native ECM (Benders et al., 2013). To date, numerous acellular ECM products, which originate from human skin, porcine

✉ Zhiwei JIANG, jzw0913@zju.edu.cn
✉ Guoli YANG, guo_li1214@zju.edu.cn
* The two authors contributed equally to this work
Zhiwei JIANG, https://orcid.org/0000-0001-8203-6151
Guoli YANG, https://orcid.org/0000-0002-1780-8757

Received May 22, 2026; Revision accepted Oct. 16, 2026;
Crosschecked xxx. xx, 20xx

© Zhejiang University Press 2026

urinary bladder, and porcine small intestinal submucosa, have shown considerable potential in regenerative applications (Abou Neel et al., 2013). Tissue-derived dECM scaffolds have also been increasingly investigated for bone regeneration; however, their composition, architecture, and mechanical properties depend strongly on the tissue of origin, making tissue–source selection a critical consideration in scaffold development.

Against this background, hard palatal mucosa (PM)—given its distinctive structural and biological characteristics—was selected as the source tissue for decellularized matrix preparation. As a mechanically adapted masticatory mucosa, PM contains a relatively thick lamina propria composed of dense, multidirectionally organized collagen fibers, providing structural stability and resistance to mechanical deformation (Iglesias-Bartolome et al., 2018). Therefore, PM was expected to retain a continuous 3D ECM framework and a certain degree of mechanical integrity after cellular removal. The collagen-rich ECM expected to remain after decellularization may provide a natural 3D microenvironment that supports cell attachment and proliferation, facilitates tissue ingrowth and new matrix deposition, thereby it potentially contributes to bone regeneration (Xu, Kankala, Wang, & Chen, 2024). Moreover, PM has been reported to exhibit ECM-organization and osteogenesis-related molecular profiles, providing additional biological support for investigating its potential in bone regeneration (Asparuhova et al., 2023). However, it remains unclear whether these structural and biological characteristics can be preserved after decellularization and translated into effective regeneration of localized bone defects.

In this study, we fabricated a decellularized PM (DPM) scaffold and systematically evaluated its decellularization efficiency, structural characteristics, ECM composition, mechanical properties, and cytocompatibility. Subsequently, we investigated its bone-regenerative potential in a rat calvarial defect model to determine the feasibility of DPM as a candidate bioactive scaffold for localized bone-defect repair, with potential future applications in alveolar ridge preservation and the repair of localized alveolar, periodontal, as well as other oral and craniofacial bone defects (Fig 1).

Unedited

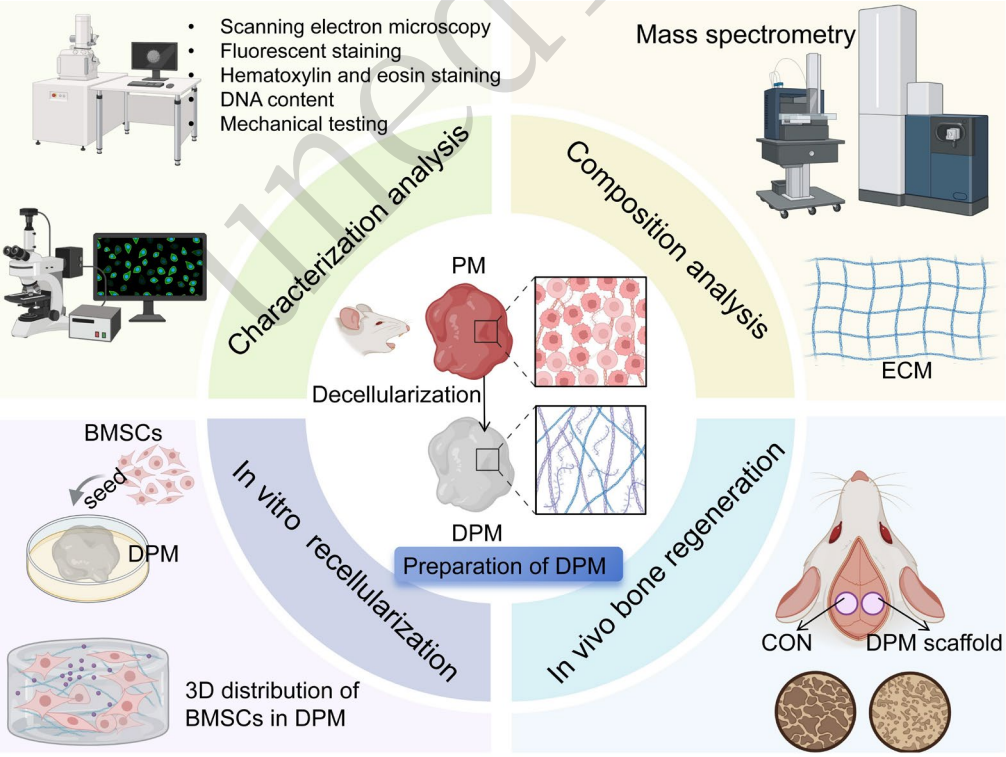


Fig. 1 Schematic diagram summarizing the key findings of this article. Created in BioRender. Jiang, Z. (2026) https://BioRender.com/1hzsfq7

2 Materials and methods

2.1 Preparation of DPM

All animal experiments were performed following the ARRIVE guidelines and were approved by the Institutional Animal Care and Use Committee of Zhejiang University (Hangzhou, China; Approval No. ZJU20250788). PM was decellularized according to the protocol developed by Ventura et al. (Ventura, Padalhin, Park, & Lee, 2019). Briefly, PM mucoperiosteal tissues (approximately 4 × 6 mm) were obtained from 8-week-old Sprague-Dawley (SD) rats under anesthesia. PM was washed thoroughly with distilled water to remove adhering dirt and debris. The cleaned PM was put into a -80℃ freezer for rapid freezing and then transferred to a 37℃ oven for thawing. The freeze-thaw process was repeated three times. The PM was exposed to 0.25% trypsin-EDTA solution for 20 h at 37℃ and washed in distilled water. Decellularization was further carried out using 0.1% SDS in 70% isopropanol at 37℃ for 24 h, followed by thorough washing with distilled water. Then, it was placed in 1% Triton X-100 prepared with 70% isopropanol and shaken at 37℃ for 18 h. The solution was refreshed every 6 h. Finally, the samples were positioned in 100% isopropanol and shaken at 37℃ for 12 h. The solution was refreshed every 4 h and washed with distilled water more than 5 times to remove all the reagents thoroughly. The sample was freeze-dried for 48 h and sterilized by ultraviolet irradiation (365 nm, 55 W/m^2) on both sides for 30 min before further use. Three independent DPM batches were prepared on separate occasions from separately collected PM tissues, with each batch undergoing the complete decellularization procedure independently. Samples from these independent preparations were included in selected characterization analyses to assess batch-to-batch consistency.

2.2 Characteristics of DPM

2.2.1 DNA content

To confirm the efficiency of the decellularization, the measurement of DNA content was carried out. Both the PM and DPM (≤25 mg) were washed thoroughly three times with phosphate-buffered saline (PBS). The Animal Tissues/Cells Genomic DNA Extraction Kit (Solarbio, Beijing, China) was used to extract the DNA. Briefly, the samples were ground into powder under liquid nitrogen, treated with RNase A and proteinase K, and purified through a spin column before DNA elution. A standard curve was generated using serially diluted standard solutions, and the DNA content of each sample was calculated based on this curve.

2.2.2 Hematoxylin and eosin (HE) staining

After washing three times with PBS, the samples were fixed in 10% formalin, embedded in paraffin, sectioned, and subjected to HE staining. The stained sections were observed under a light microscope (CKX41, Olympus, Japan).

2.2.3 Scanning electron microscopy (SEM)

Both PM and DPM were fixed in 2.5% glutaraldehyde for 60 min and washed thoroughly 3 × for 15 min each. Then, the samples were dehydrated in a gradient series of alcohol for 15 min. Next, they were dried at critical point and coated with Au/Pd. Electron microscope images were taken using a JEOL JSM-6335F field emission SEM (JEOL, Japan).

2.2.4 Fluorescent staining

Samples were fixed in 4% paraformaldehyde (Sigma-Aldrich, MO, USA) and permeabilized with 0.5% Triton X-100 (Sigma-Aldrich, MO, USA). After blocking with bovine serum albumin (BSA; Sigma-Aldrich, USA), the samples were incubated with primary antibodies against collagen I, collagen IV, fibronectin, and laminin (all diluted 1:100; Proteintech, USA), followed by the corresponding fluorescent secondary antibodies (1:200; Invitrogen, USA). Nuclei were counterstained with DAPI (Beyotime, Shanghai, China) for 5 min. Fluorescence images were acquired using a fluorescence microscope (DM4000; Leica, Germany).

Unedited

2.2.5 Mechanical testing

Mechanical testing was performed before DPM lyophilization. Following decellularization and thorough rinsing with ddH_2O, DPM specimens were tested directly in the hydrated state. Native PM specimens were also tested under hydrated conditions using the same compression protocol. The compressive properties of PM and DPM were evaluated using a universal testing machine (Instron 5967, Instron, USA). Load-displacement curves were recorded during compression testing, and Young's modulus and maximum load were obtained from the testing system.

2.2.6 Mass spectrometry

Proteins were extracted from PM and DPM samples and digested with trypsin. The resulting peptides were separated using a NanoElute ultra-high-performance liquid chromatography system and analyzed using a timsTOF Pro mass spectrometer in parallel accumulation−serial fragmentation mode. Protein abundance was assessed using label-free quantification (LFQ).

2.3 Culture and characterization of rat BMSCs

Male SD rats (4-week-old) were employed to isolate and culture the bone marrow mesenchymal stem cells (BMSCs) as described previously (Lennon & Caplan, 2006). BMSCs were cultured in basal medium including α-MEM (BI, Israel) containing 10% fetal bovine serum (FBS; Gibco, United States), 0.272 g/L L-glutamine (Sigma, United States), 1% penicillin (Gibco, United States), and 1% streptomycin (Gibco, United States). Passage-2 rat BMSCs were resuspended in PBS at (1×10^6) cells/mL and stained with PE-conjugated anti-rat CD90 (E-AB-F1226D), CD44H (E-AB-F1225D), CD29 (E-AB-F1309D), or CD45 (E-AB-F1227D) antibodies (Elabscience, China) for 30 min at 4℃ in the dark. CD34 was detected using an unconjugated rabbit anti-rat CD34 antibody (98069-1-RR; Proteintech, China), followed by an Alexa Fluor 488-conjugated anti-rabbit IgG secondary antibody. After two washes with PBS, the cells were analyzed using a CytoFLEX LX flow cytometer (Beckman Coulter, USA). Unstained cells were used to define positive gates, and debris and doublets were excluded before calculating marker-positive percentages.

2.4 In vitro evaluation of DPM

2.4.1 Recellularization

The recellularization potential of DPM was evaluated using rat BMSCs. A total of 2×10^5 cells suspended in 100 μL of complete culture medium were seeded onto each DPM scaffold. To facilitate initial cell attachment, the scaffolds were incubated at 37℃ for 30 min. Additional complete culture medium was then gently added to a final volume of 2 mL per well, and the constructs were cultured for 3 days. Subsequently, the scaffolds were gently washed with PBS, fixed with 4% paraformaldehyde for 30 min, and stained with a ready-to-use DAPI solution (Thermo Fisher Scientific, USA) to visualize the cell nuclei. Cell-free DPM scaffolds subjected to the same fixation and staining procedures were used as negative controls. Z-stack images were acquired using a Zeiss laser-scanning confocal microscope equipped with Airyscan 2 (Carl Zeiss, Germany) and a 63× oil-immersion objective, followed by 3D reconstruction.

2.4.2 Cell proliferation

Cell proliferation was evaluated with Alamar blue (Invitrogen, Carlsbad, CA). BMSCs were washed three times with PBS, and a medium containing 10% Alamar blue was added to each well. The wells were incubated for 4 h at 37℃. Fluorescence intensity was measured using a microplate reader with a 540 nm excitation filter and a 590 nm emission filter.

2.4.3 Quantitative real-time PCR

Total RNA was extracted by TRIzol® reagent (Thermo-Fischer Scientific, USA) in accordance with the

Unedited

manufacturer's instructions. Quantitative real-time PCR was carried out to detect the expression of mRNA using TB Green PCR Mix (TaKaRa) in the 384 Real-Time PCR System (Bio-Rad, USA). The mRNA expression of Low-density lipoprotein receptor-related protein 5 (LRP5), Runt-related transcription factor 2 (Runx2), Osterix (OSX), Bone morphogenetic protein 2 (BMP2), Osteocalcin (OCN), and Glyceraldehyde-3-phosphate dehydrogenase (GAPDH) were detected after 7 days and 14 days in the BMSCs group (control group) and the BMSCs + DPM group (DPM group), respectively (Table S1).

2.5 In vivo evaluation of DPM

2.5.1 Surgical procedure

Twelve 8-week-old SD rats were used for the animal experiments. A rat calvarial defect model was established as described previously (Y. N. Zhang, Feng, Shao, Jiang, & Yang, 2023). Briefly, a full-thickness skin flap and periosteum were elevated to expose the calvarium. Two bilateral full-thickness calvarial defects with a diameter of 5 mm were created using a trephine bur under continuous saline irrigation. DPM was implanted into the right calvarial defect (DPM group), while the left defect was left untreated as the control (Fig. 5a-b). All rats received intramuscular penicillin once daily for 3 days after surgery.

2.5.2 Micro-computed tomography (CT) analysis

At 4 and 8 weeks after surgery, the harvested calvarial specimens were fixed in 4% paraformaldehyde for 48 h and subsequently transferred to 75% ethanol until micro-CT scanning. The specimens were scanned using a μCT 100 system (SCANCO Medical AG, Switzerland) at an isotropic voxel size of 20 μm. The scanning parameters were set to 70 kV, 200 μA, and an integration time of 300 ms. A 5-mm-diameter cylindrical region corresponding to the original calvarial defect was defined as the region of interest. Bone volume fraction (BV/TV), trabecular thickness (Tb.Th), and trabecular separation (Tb.Sp) within the region of interest were calculated using Evaluation software version 6.6 (SCANCO Medical AG, Switzerland).

2.5.3 Histological analysis

After micro-CT scanning, the calvarial specimens were decalcified in 10% EDTA, embedded in paraffin, and sectioned at a thickness of 5 μm. Sections through the central region of the defects were subjected to HE and Masson’s trichrome staining and examined using a light microscope (CKX41, Olympus, Japan).

2.5.4 Immunohistochemical analysis

Sections collected at 4 weeks were incubated with primary antibodies against ALP (catalog No. GB11527; Servicebio, Wuhan, China; 1:500) and BMP2 (catalog No. GB15252; Servicebio; 1:500), whereas sections collected at 8 weeks were incubated with primary antibodies against OCN (catalog No. GB11233; Servicebio; 1:500) and BMP2 (catalog No. GB15252; Servicebio; 1:500). Color development was performed using DAB, followed by hematoxylin counterstaining. Images were acquired using a light microscope (CKX41; Olympus, Japan). The positive area within the defect region was quantified using ImageJ software, with identical threshold settings across the two groups for each marker and expressed as a percentage of the tissue area. Six defects per group were analyzed at each time point (n = 6).

2.6 Statistical analysis

All quantitative analyses were performed in a blinded manner. Data were presented as mean ± standard deviation (SD). For the in vitro experiments, comparisons between two independent groups were performed using unpaired Student’s t-test. For the in vivo experiments, because DPM-treated and untreated defects were created bilaterally in the same animals, paired Student’s t-test was used to compare the two groups at each time point. The in vitro experiments were performed with 3–5 biological replicates and repeated three times independently. For the in vivo experiments, six animals were included at each time point. A value of $P < 0.05$ was considered statistically significant.

Unedited

3 Results

3.1 Characteristics of DPM

Gross observation, HE staining, DNA quantification, SEM, immunofluorescence staining, and compression testing were performed to evaluate the decellularization efficiency, structural and compositional characteristics, and mechanical properties of DPM. Rat hard PM was located in the anterior part of the maxilla, and showed obvious palatal folds on the surface (Fig. 2a). Fresh PM appeared pink and opaque, with a relatively tough texture and a certain degree of elasticity (Fig. 2b). DPM appeared white and semi-transparent, with a softer texture and slightly reduced elasticity (Fig. 2c). No obvious change in gross size was observed before and after decellularization. HE staining showed the absence of visible nuclei in DPM compared with PM (Figs. 2d, e). DNA quantification further confirmed the efficiency of decellularization. The DNA content decreased from 1,222.85 ± 109.7 ng/mg in PM to 10.48 ± 6.62 ng/mg in DPM ($P < 0.001$) (Fig. 2f). SEM showed that both PM and DPM retained an intact 3D architecture without obvious collapse. PM exhibited a keratinized layer, whereas no obvious keratinized layer was observed in DPM. PM was composed of irregularly arranged fiber bundles. Compared with PM, DPM showed slightly fewer filamentous fibers and slightly larger pores between fiber bundles. No cells were observed on the surface of DPM (Fig. 2g). The immunofluorescence staining of collagen I, collagen IV, fibronectin, and laminin indicated that the major ECM components were largely preserved after decellularization. The absence of DAPI staining in DPM further confirmed effective removal of cellular components (Fig. 2h). Compression testing under hydrated conditions showed differences in the compressive responses of PM and DPM (Fig. 2i). The Young's modulus of DPM was significantly higher than that of native PM ($P < 0.05$; Fig. 2j), whereas no significant difference in maximum load was observed between the two groups (Fig. 2k).

unedited

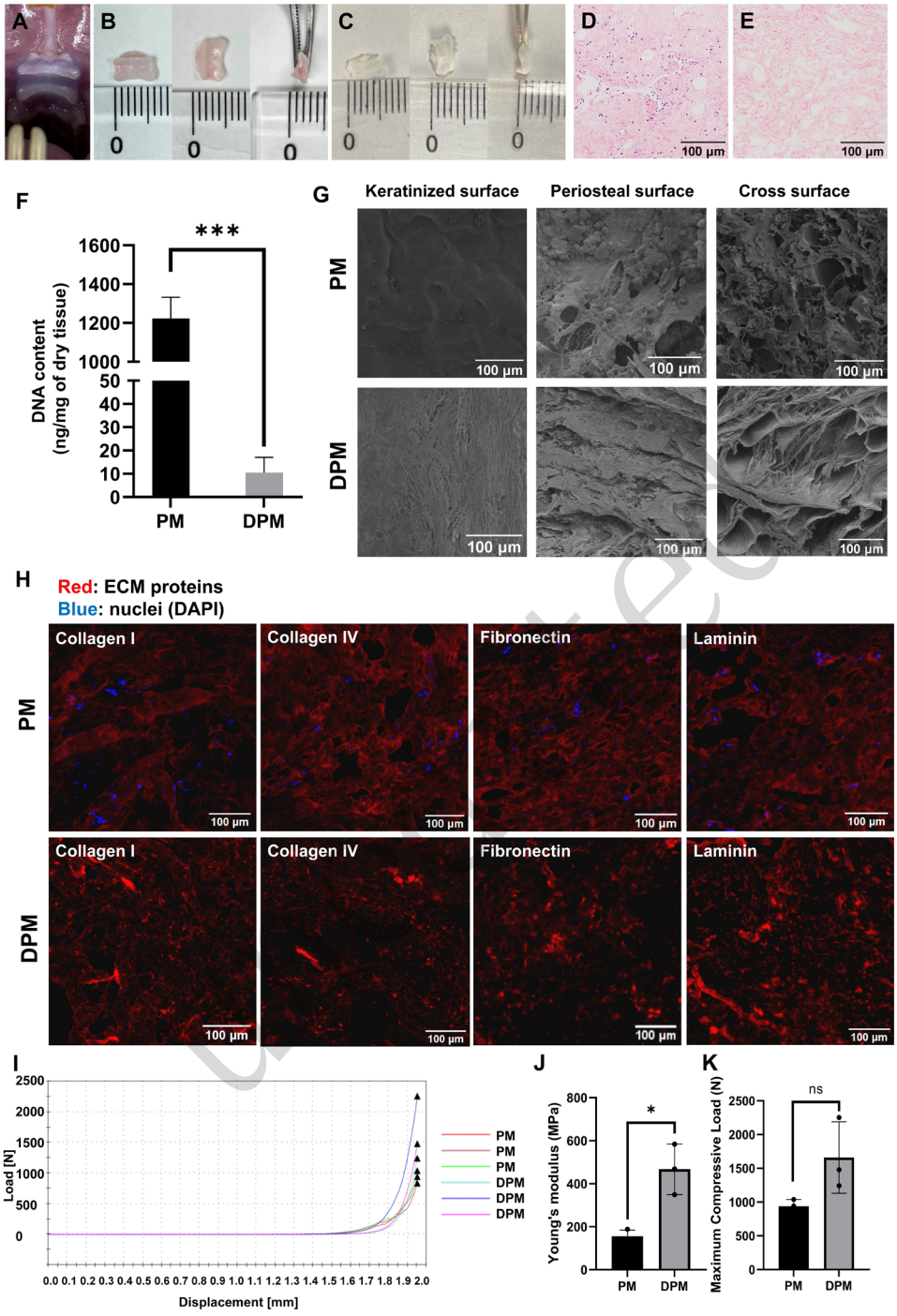


Fig. 2 Characteristics of PM and DPM. (A) Position of the hard PM. (B) Representative images of PM. (C) Representative images of DPM. (D, E) HE staining of PM and DPM. Scale bar = 100 μm. (F) DNA content of PM and DPM. $^{***}P < 0.001$. n = 3. (G) SEM images of PM and DPM. Scale bar = 100 μm. (H) Immunofluorescence staining of collagen I, collagen IV, fibronectin, and laminin in PM and DPM. The indicated ECM proteins are shown in red, and cell nuclei counterstained with DAPI are shown in blue. Scale bars = 100 μm. (I) Representative load-displacement curves obtained from compression testing. (J) Quantitative analysis of Young's modulus. Data are expressed as mean ± SD. $^{*}P < 0.05$. n = 3. (K) Quantitative analysis of maximum load. n = 3.

3.2 Composition of PM and DPM

Mass spectrometry was performed to assess the composition of PM and DPM. A total of 4,934 proteins were identified in native PM, with 4,873, 4,881 and 4,881 proteins detected in the three PM samples, respectively. Among them, 705 extracellular proteins accounted for 24.15% of the total protein abundance based on label-free quantification (LFQ) values. Cytoplasmic proteins (2,486 proteins), nuclear proteins (1,206 proteins), and plasma membrane proteins (537 proteins) accounted for 41.32%, 31.33%, and 3.19% of the total abundance based on LFQ values, respectively. The number of identified protein species in DPM was significantly lower than that in PM ($P < 0.05$). A total of 2,934 proteins were identified in DPM, with 2,576, 2,527 and 2,493 proteins detected in the three DPM samples, respectively. Extracellular proteins (441 proteins), cytoplasmic proteins (1,544 proteins), nuclear proteins (610 proteins), and plasma membrane proteins (339 proteins) accounted for 56.79%, 20.68%, 17.62%, and 4.91% of the total abundance based on LFQ values, respectively.

Furthermore, analysis of the complexity and abundance of ECM proteins was conducted. The five most abundant extracellular proteins in PM were Albumin (ALB), Collagen alpha-2[I] chain (COL1A2), Collagen alpha-1[I] chain (COL1A1), Decorin (DCN), and Murinoglobulin-1 (MUG1), with contents of 31.88%, 14.75%, 14.48%, 1.45%, and 1.33%, respectively (Table S2). Glycoproteins represented the largest extracellular protein subcategory in PM (96 proteins, 48.41%). Among them, ALB, MUG1, LAMA2, and Alpha-2-HS glycoprotein (AHSG) were the most abundant proteins. Collagens represented the second most abundant extracellular protein subcategory, accounting for 31.59% of the total extracellular protein abundance. Proteoglycans (26 proteins, 7.90%), ECM-affiliated proteins (29 proteins, 2.67%), regulators (25 proteins, 2.34%), and secreted factors (8 proteins, 1.54%) were detected. The five most abundant extracellular proteins in DPM were COL1A2, COL1A1, Laminin subunit alpha 2 (LAMA2), Collagen alpha-1[III] chain (COL3A1), and Mast cell protease 1 (MCPT1), with contents of 44.43%, 41.06%, 4.03%, 2.60%, and 1.35%, respectively (Table S3). Collagens represented the dominant extracellular protein subcategory in DPM (15 proteins, 89.70%), among which COL1A2, COL1A1, COL3A1, COL5A2, and COL5A3 were the most abundant. The proportion of glycoproteins decreased to 5.67%, and that of ECM-affiliated proteins decreased to 1.06% in DPM (Fig. 3).

uncorrected

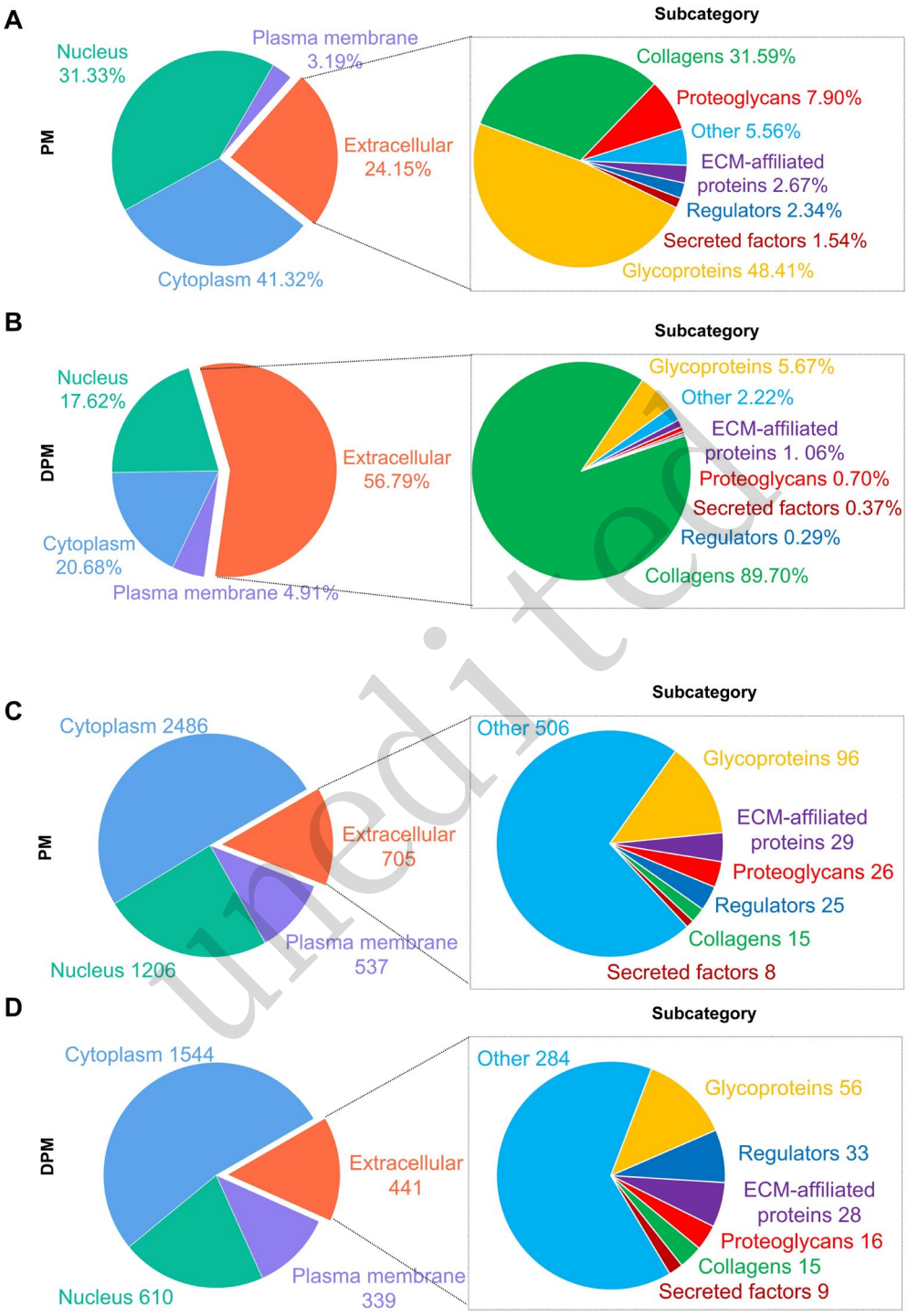


Fig. 3 Composition of PM and DPM. (A) LFQ% for nucleus, cytoplasm, plasma membrane, and extracellular proteins of PM, and further classification of extracellular proteins based on function and subcategory. (B) LFQ% for nucleus, cytoplasm, plasma membrane, and extracellular proteins of DPM, and further classification of extracellular proteins based on function and subcategory. (C) Classification of PM proteins and extracellular protein subcategories based on protein numbers. (D) Classification of DPM proteins and extracellular protein subcategories based on protein numbers.

unedited

3.3 DPM supported BMSC recellularization, proliferation and osteogenic response in vitro

Flow cytometry showed that passage-2 rat BMSCs were highly positive for CD90 (99.97%), CD44H (99.82%) and CD29 (99.88%) but exhibited low expression of CD45 (4.71%) and CD34 (5.80%) (Fig. 4a), consistent with a BMSC immunophenotype. 3D confocal imaging showed no detectable DAPI signal in the cell-free DPM control, indicating negligible background fluorescence in the DAPI channel (Fig. 4b). In contrast, numerous individually distinguishable DAPI-stained nuclei were observed throughout the imaged region of BMSC-seeded DPM after 3 days of culture (Fig. 4c), confirming the attachment and spatial distribution of rat BMSCs on the scaffold. In addition, the viability of BMSCs cultured with DPM was significantly higher than that of the control group at days 3, 5, and 7 ($P < 0.01$), indicating that DPM exhibited favorable cytocompatibility and supported cell proliferation in vitro (Fig. 4d).

At day 7, there was a significant upregulation of mRNA levels for osteogenic genes including LRP5 ($P < 0.05$), Runx2 ($P < 0.05$), OSX ($P < 0.001$), BMP2 ($P < 0.001$), and OCN ($P < 0.001$) in the DPM group. At day 14, the expression of LRP5 ($P < 0.05$), OSX ($P < 0.05$), BMP2 ($P < 0.01$), and OCN ($P < 0.001$) was higher in the DPM group, along with a modest rise in Runx2 expression without statistical difference (Fig. 4e). These findings suggest that DPM enhanced the osteogenic response of BMSCs in vitro.

unedited

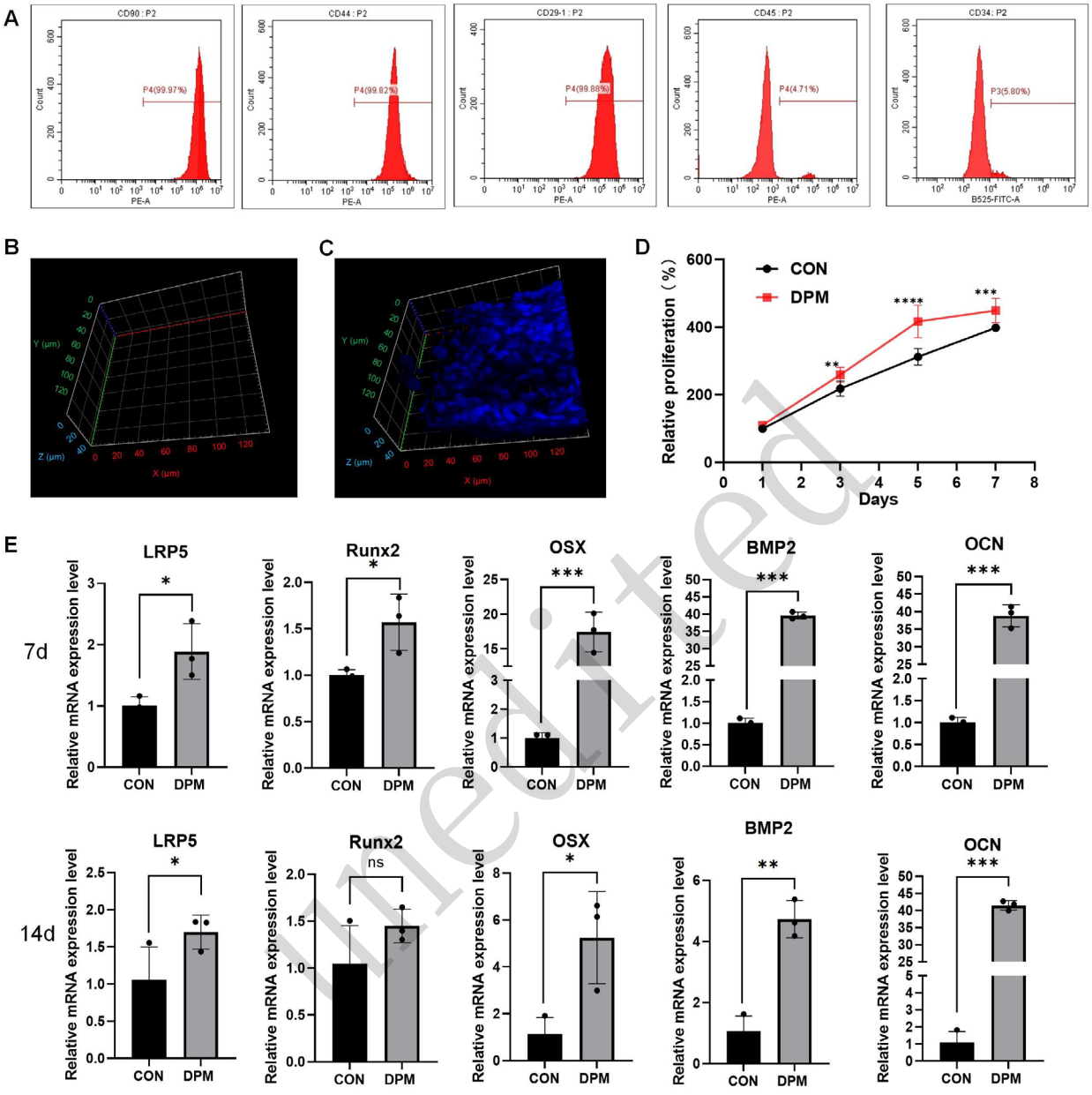


Fig. 4 Characterization and in vitro cellular responses of rat BMSCs cultured with DPM. (A) Flow cytometric characterization of rat BMSCs. (B, C) Representative 3D confocal reconstructions of cell-free DPM and BMSC-seeded DPM after 3 days of culture. BMSC nuclei were stained with DAPI (blue). (D) Relative proliferation of BMSCs in the control and DPM groups at days 1, 3, 5, and 7. (E) Relative mRNA expression of osteogenesis-related genes in the control and DPM groups after 7 and 14 days of osteogenic induction. Data are expressed as mean ± SD. $^{*}P < 0.05$, $^{**}P < 0.01$, $^{***}P < 0.001$, $^{****}P < 0.0001$.

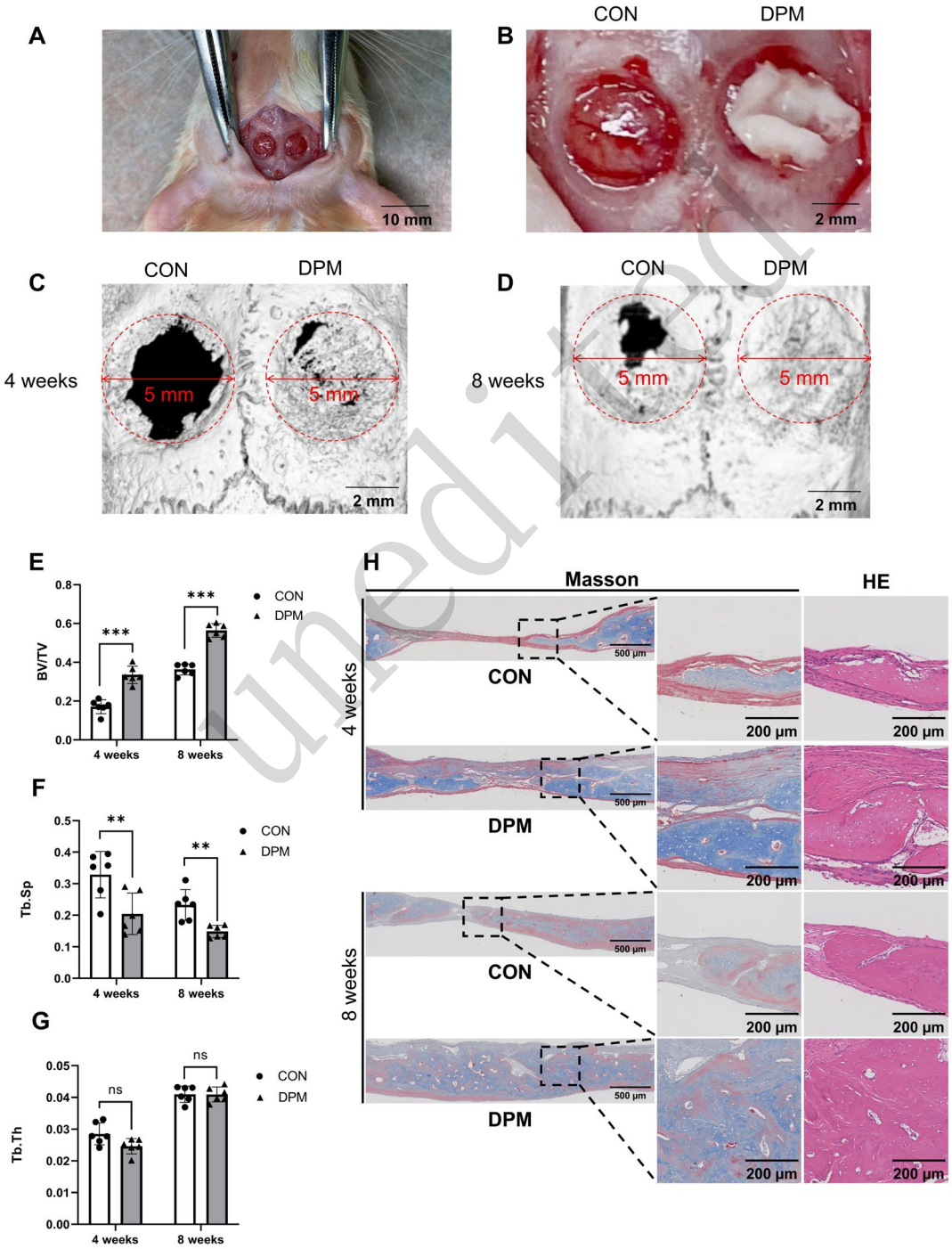
3.4 DPM promoted bone regeneration in vivo

More extensive new bone formation was observed in the DPM group than in the control group at both 4 and 8 weeks (Fig. 5c-d). BV/TV was significantly higher in the DPM group than that in the control group after 4 and 8 weeks ($P < 0.001$) (Fig. 5e). Tb.Sp was significantly lower in the DPM group than that in the control group after 4 and 8 weeks ($P < 0.01$) (Fig. 5f). There were no statistical differences in Tb.Th between the two

Unedited

groups after 4 and 8 weeks (Fig. 5g). HE and Masson staining results showed that a small region of newly formed bone was scattered adjacent to the calvarial defects in the control group, while there was abundant, dense and widely distributed newly formed bone around the defect region in the DPM group after 4 and 8 weeks (Fig. 5h).

Immunohistochemical staining indicated that the positive areas of ALP and BMP2 at 4 weeks and those of OCN and BMP2 at 8 weeks were significantly greater in the DPM group than in the control group (all $P < 0.05$; Fig. 6). These findings provide local protein-level evidence of enhanced osteogenic activity in the DPM-treated defects.



Unedited

Fig. 5 DPM promoted bone regeneration in vivo. (A) Representative intraoperative photographs of bilateral 5-mm full-thickness calvarial defects before and (B) after DPM implantation. CON indicates the untreated control defect and DPM indicates the contralateral defect implanted with DPM. Scale bars = 10 mm in (A) and 2 mm in (B). (C-D) Representative micro-CT images of untreated control (CON) and DPM-treated defects at 4 and 8 weeks. The red dashed circles and arrows indicate the original defect boundaries and diameters (5 mm), respectively. Scale bars = 2 mm. (E, F, G) BV/TV, Tb.Sp, and Tb.Th were measured. n = 6. ns, not significant; Data are expressed as mean ± SD. $^{*}P < 0.05$, $^{**}P < 0.01$, and $^{***}P < 0.001$. (H) Representative Masson's trichrome and HE staining of defects in the CON and DPM groups at 4 and 8 weeks. Scale bar = 500 μm (left). Scale bar = 200 μm (right).

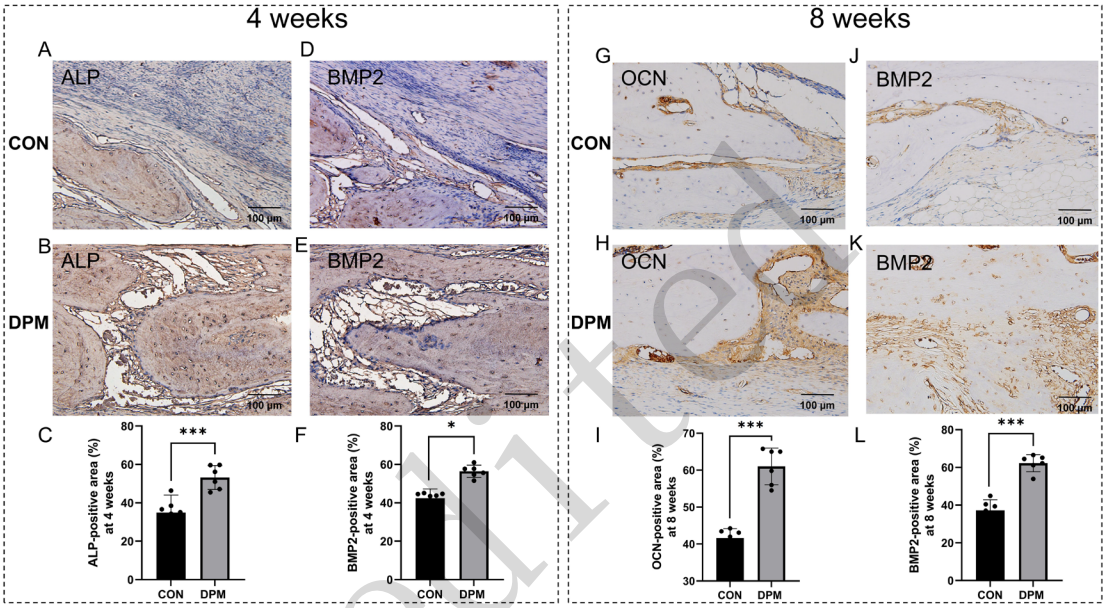


Fig. 6 Immunohistochemical evaluation of osteogenesis-related proteins in calvarial defects. (A–F) Representative staining and quantification of ALP and BMP2 at 4 weeks and (G–L) OCN and BMP2 at 8 weeks. Brown indicates positive staining and blue indicates hematoxylin-counterstained nuclei. Data are presented as mean ± SD (n = 6). Scale bars = 100 μm. $^{*}P < 0.05$ and $^{***}P < 0.001$.

unedited

4 Discussion

In this study, we successfully prepared a decellularized scaffold derived from PM using a standardized decellularization protocol. DPM effectively removed most cellular components while largely preserving the native extracellular matrix architecture and major matrix-associated components. In addition, DPM supported BMSC recellularization, proliferation and osteogenesis-related gene expression in vitro and promoted bone regeneration in a rat calvarial defect model. These findings suggest that DPM may serve as a promising bioactive scaffold for bone defect repair.

Decellularized extracellular matrix-based biomaterials have attracted increasing interest in regenerative medicine and tissue engineering as they provide a structural framework together with retained biological cues from native tissues (Li, Javed, & Ao, 2021). In previous studies, researchers set up a scaffold derived from decellularized porcine mucoperiosteum, which might be suitable for allogeneic transplantation and cleft lip and

palate repair (Rizzo et al., 2021). In another experiment, it was illustrated that a scaffold generated from human palatal gingival tissue is a suitable substrate for blastema cell migration and activity (Naderi et al., 2013). Compared with these studies, our work further demonstrated the potential of a hard PM-derived decellularized scaffold in bone regeneration, supported by both in vitro evaluation and in vivo evidence. We also used a combination of physical, chemical and enzymatic treatments to prepare DPM. The decellularization protocol was selected to balance effective cellular removal with the preservation of extracellular matrix structure and protein components (Huang et al., 2023). This strategy helped preserve the structural and biological characteristics of the scaffold.

Our findings provide experimental support for selecting PM as a source tissue for decellularized scaffold preparation. First, DPM maintained a continuous 3D architecture without obvious collapse and retained measurable mechanical resistance under hydrated conditions, indicating that the structurally stable and mechanically adapted characteristics of native PM were partly preserved after decellularization (Iglesias-Bartolome et al., 2018). Second, proteomic analysis showed an enrichment of extracellular proteins in DPM. The predominance of collagen, particularly types I and III, may provide a framework for cell attachment, tissue ingrowth and new matrix deposition, while retained collagen IV, fibronectin, laminin, glycoproteins, and proteoglycans may create additional adhesion sites and matrix-associated cues for cell–ECM interactions (X. Zhang et al., 2022). Consistent with the reported ECM–organization and regeneration-related characteristics of palatal connective tissue (Asparuhova et al., 2023), DPM supported BMSC attachment, proliferation and osteogenesis-related gene expression in vitro and promoted bone formation in vivo. Third, PM is surgically accessible and its donor site generally demonstrates favorable healing with limited scar formation (Han et al., 2020). Fourth, its relatively thin, continuous and sheet-like structure facilitates the diffusion of decellularization reagents and subsequent washing while allowing the scaffold to retain sufficient integrity for handling and implantation. Finally, DPM can be trimmed and adapted to localized defects and may therefore represent an underexplored tissue-derived scaffold for alveolar ridge preservation and the repair of localized alveolar, periodontal and other oral and craniofacial bone defects.

Interestingly, DPM exhibited a higher Young's modulus than native PM under hydrated testing conditions. Decellularization can alter tissue mechanics by changing ECM composition, microstructure, porosity, and fiber interactions, although the magnitude and direction of these changes depend on the tissue source and decellularization protocol (Franko et al., 2024; X. Zhang et al., 2022). In our study, the removal of cellular and soluble components may have increased the relative contribution of the retained collagen-rich ECM network to load bearing. Decellularization-induced changes in ECM organization, interfibrillar interactions and load-transfer behavior may also have contributed to the increased resistance to compressive deformation (Girardeau-Hubert et al., 2022). Nevertheless, the maximum load did not differ significantly between PM and DPM, indicating that the increased Young's modulus represents greater stiffness rather than improved overall load-bearing capacity. Because ECM organization and fiber interactions were not directly quantified, the underlying mechanism remains to be clarified.

unedited

Several limitations in this study must be noted. First, tissue availability and xenogeneic immunogenicity are major translational limitations of DPM. Although PM is surgically accessible, the amount of autologous tissue that can be safely harvested is limited and may be insufficient for larger defects (Aguirre-Zorzano, García-De La Fuente, Estefanía-Fresco, & Marichalar-Mendía, 2017). Porcine or bovine PM may provide more abundant sources but can introduce xenogeneic immunogenicity concerns. Before xenogeneic translation, the effectiveness of decellularization should be evaluated by quantifying residual DNA and determining whether relevant xenoantigens remain within the ECM, particularly galactose-α-1,3-galactose and N-glycolylneuraminic acid (Kasravi et al., 2023). Immunologically relevant models should be created to characterize both early and late local immune responses, including macrophage polarization, lymphocyte infiltration, foreign-body giant-cell formation, fibrosis, and tissue remodeling. Systemic humoral responses, including xenoantigen-specific IgM and IgG production and complement activation, should also be assessed to establish the immunological safety (Gasek et al., 2021). Second, no clinically used xenogeneic decellularized matrix was included as a positive comparator. Consequently, although DPM showed bone-regenerative potential relative to untreated defects, its efficacy and safety relative to existing commercial materials remain unknown. Third, DPM was evaluated only in a rat calvarial defect model, which does not fully reproduce the clinical conditions of alveolar ridge preservation, periodontal bone-defect repair, or other oral and craniofacial bone defects. Therefore, further validation is required through models that more closely reflect the intended applications.

5 Conclusions

To sum up, we successfully prepared a decellularized scaffold derived from PM by a standardized, time-efficient and reproducible decellularization protocol. DPM retained most of the ECM components and removed most of the cellular components. DPM supported BMSC recellularization, proliferation and osteogenesis-related gene expression in vitro and promoted bone regeneration in rat calvarial defects. These findings support the potential of DPM as a bioactive scaffold for localized bone-defect repair.

Data availability statement

The data that support the findings of this study are available from the corresponding author upon reasonable request.

Acknowledgments

This work was supported by the the Science and Technology Program of Zhejiang Province (Grant Number: 2024C03194) and National Natural Science Foundation of China (Grant Nos: U24A20711).

Author contributions

Jin HE and Lingfei REN performed the experimental research and data analysis, wrote and edited the manuscript. Jin HE, Lingfei REN, and Xueting Wang performed the establishment of animal models. Mengdie FU and Qifeng JIANG contributed to data analysis. Zhiwei JIANG and Guoli YANG contributed to the study design and editing of the manuscript. All authors have read and approved the final manuscript, and therefore, have full access to all the data in the study and take responsibility for the integrity and security of the data.

unedited

Compliance with ethics guidelines

Jin HE, Lingfei REN, Mengdie FU, Qifeng JIANG, Xueting WANG, Zhiwei JIANG, and Guoli YANG declare that they have no conflicts of interest.

All institutional and national guidelines for the care and use of laboratory animals were followed. All animal procedures were reviewed and approved by the Laboratory Animal Welfare and Ethics Review Committee of Zhejiang University (Approval No. ZJU20250788).

Declaration on the use of generative AI tools

During the preparation and revision of this manuscript, the authors used OpenAI ChatGPT (GPT-5) for English language polishing and improving the clarity, conciseness, and academic style of the manuscript and responses to reviewers. The prompts mainly requested grammatical correction, refinement of academic expression, and improvement of textual organization without altering the scientific meaning. The tool was used in May and September 2026. Relevant records, generated content, and the revision process have been preserved and can be provided for editorial review upon request. All AI-generated output was thoroughly reviewed, verified, and edited by the authors. The authors take full responsibility for the accuracy, originality, and final content of the submitted manuscript.

References

Abou Neel, E. A., Bozec, L., Knowles, J. C., Syed, O., Mudera, V., Day, R., et al., 2013. Collagen - Emerging collagen based therapies hit the patient. *Advanced Drug Delivery Reviews, 65*(4):429-456.

Aguirre-Zorzano, L. A., García-De La Fuente, A. M., Estefanía-Fresco, R., & Marichalar-Mendia, X., 2017. Complications of harvesting a connective tissue graft from the palate. A retrospective study and description of a new technique. *J Clin Exp Dent, 9*(12):e1439-e1445.

Asparuhova, M. B., Song, X., Riedwyl, D., van Geest, G., Bosshardt, D. D., & Sculean, A., 2023. Differential molecular profiles and associated functionalities characterize connective tissue grafts obtained at different locations and depths in the human palate. *Int J Oral Sci, 15*(1):57.

Bae, S. E., Bhang, S. H., Kim, B. S., & Park, K., 2012. Self-Assembled Extracellular Macromolecular Matrices and Their Different Osteogenic Potential with Preosteoblasts and Rat Bone Marrow Mesenchymal Stromal Cells. *Biomacromolecules, 13*(9):2811-2820.

Benders, K. E. M., van Weeren, P. R., Badylak, S. F., Saris, D. B. F., Dhert, W. J. A., & Malda, J., 2013. Extracellular matrix scaffolds for cartilage and bone regeneration. *Trends in Biotechnology, 31*(3):169-176.

Franko, R., Franko, Y., Ribes Martinez, E., Ferronato, G. A., Heinzelmann, I., Grechi, N., et al., 2024. Mechanical properties of native and decellularized reproductive tissues: insights for tissue engineering strategies. *Sci Rep, 14*(1):7347.

Gasek, N., Dearborn, J., Enes, S. R., Pouliot, R., Louie, J., Phillips, Z., et al., 2021. Comparative immunogenicity of decellularized wild type and alpha 1,3 galactosyltransferase knockout pig lungs. *Biomaterials, 276:*121029.

Girardeau-Hubert, S., Lynch, B., Zuttion, F., Label, R., Rayee, C., Brizion, S., et al., 2022. Impact of microstructure on cell behavior and tissue mechanics in collagen and dermal decellularized extra-cellular matrices. *Acta Biomater, 143:*100-114.

Han, N. N., Jia, L., Guo, L. J., Su, Y. Y., Luo, Z. H., Du, J., et al., 2020. Balanced oral pathogenic bacteria and probiotics promoted wound healing via maintaining mesenchymal stem cell homeostasis. *Stem Cell Research & Therapy, 11*(1):66.

Huan, Y., Chen, H. Q., Zhou, D. Z., Hie, X., Li, S. Z., Wu, X. Q., et al., 2025. Concurrently bioprinted scaffolds with autologous bone and allogeneic BMSCs promote bone regeneration through native BMSC recruitment. *Bio-Design and Manufacturing, 8*(1):85-99.

Huang, X. T., Ding, Z., Feng, R. X., Zheng, X., Yang, N., Chen, Y. N., et al., 2023. Balanced chemical reactivity, antimicrobial properties and biocompatibility of decellularized dermal matrices for wound healing. *Soft Matter, 19*(48):9478-9488.

Iglesias-Bartolome, R., Uchiyama, A., Graf, R., Molinolo, A. A., Abusleme, L., Brooks, S. R., et al., 2018. Unique transcriptional signature primes oral mucosa for rapid wound healing in humans. *Journal of Investigative Dermatology, 138*(5):S237-S237.

Jung, J. P., Bhuiyan, D. B., & Ogle, B. M., 2016. Solid organ fabrication: comparison of decellularization to 3D bioprinting. *Biomaterials research, 20*(1):27.

Kasravi, M., Ahmadi, A., Babajani, A., Mazloomnejad, R., Hatamnejad, M. R., Shariatzadeh, S., et al., 2023. Immunogenicity of decellularized extracellular matrix scaffolds: a bottleneck in tissue engineering and regenerative medicine. *Biomater Res, 27*(1):10.

Lau, C. S., Hassanbhai, A., Wen, F., Wang, D. A., Chanchareonsook, N., Goh, B. T., et al., 2019. Evaluation of decellularized tilapia skin as a tissue engineering scaffold. *Journal of Tissue Engineering and Regenerative Medicine, 13*(10):1779-1791.

Lennon, D. P., & Caplan, A. I., 2006. Isolation of rat marrow-derived mesenchymal stem cells. *Experimental Hematology, 34*(11):1606-1607.

Li, T., Javed, R., & Ao, Q., 2021. Xenogeneic Decellularized Extracellular Matrix-based Biomaterials For Peripheral Nerve Repair and Regeneration. *Current Neuropharmacology, 19*(12):2152-2163.

Lichte, P., Pape, H. C., Pufe, T., Kobbe, P., & Fischer, H., 2011. Scaffolds for bone healing: Concepts, materials and evidence. *Injury-International Journal of the Care of the Injured, 42*(6):569-573.

unedited

Naderi, S., Zadeh, J. K., Shahri, N. M., Abady, K. N. S., Cheravi, M., Baharara, J., et al., 2013. Three-Dimensional Scaffold from Decellularized Human Gingiva for Cell Cultures: Glycoconjugates and Cell Behavior. *Cell Journal, 15*(2):166-175.

Rizzo, M. I., Tomao, L., Tedesco, S., Cajozzo, M., Esposito, M., De Stefanis, C., et al., 2021. Engineered mucoperiosteal scaffold for cleft palate regeneration towards the non-immunogenic transplantation. *Scientific Reports, 11*(1):14570.

Szpalski, C., Barr, J., Wetterau, M., Saadeh, P. B., & Warren, S. M., 2010. Cranial bone defects: current and future strategies. *Neurosurgical Focus, 29*(6):E8.

Ventura, R. D., Padalhin, A. R., Park, C. M., & Lee, B. T., 2019. Enhanced decellularization technique of porcine dermal ECM for tissue engineering applications. *Materials Science and Engineering C-Materials for Biological Applications, 104*:109841

Xu, P., Kankala, R. K., Wang, S., & Chen, A., 2024. Decellularized extracellular matrix-based composite scaffolds for tissue engineering and regenerative medicine. *Regen Biomater, 11*:rbad107.

Zhang, X., Chen, X., Hong, H., Hu, R., Liu, J., & Liu, C., 2022. Decellularized extracellular matrix scaffolds: Recent trends and emerging strategies in tissue engineering. *Bioact Mater, 10*:15-31.

Zhang, Y. N., Feng, Y. T., Shao, Q., Jiang, Z. W., & Yang, G. L., 2023. Rapid formation of 3D: Decellularized extracellular matrix spheroids for enhancing bone formation. *Journal of Biomedical Materials Research Part A, 111*(3):378-388.

Supplementary information

Tables S1–S3

unedited